WATER TEMPERATURE PREDICTION MODEL FOR OVERHEAD AQUEDUCTS WITH EXTERNAL THERMAL INSULATION MATERIALS

Guang LIU[1 2, 3*], Weiji JIANG [1], Zhenhua ZHANG [1], Yujie SONG [1], Henghui XU [1]

[1] School of Civil Engineering, Hefei University of Technology, Hefei, Anhui 230009, China

[2] Key Laboratory of Rock Mechanics and Geohazards of Zhejiang Province, Shaoxing, Zhejiang 312000, China

[3] State Key Laboratory of Safety and Health for Metal Mines, Maanshan, Anhui 243000, China

* Corresponding author; guang_liu@hfut.edu.cn

Water temperature prediction for overhead aqueducts is the basis for analyzing ice conditions and developing winter thermal insulation schemes for aqueducts. In this research, we propose an enhanced water temperature model that accounts for the coupled heat transfer processes in overhead aqueducts, incorporating water, aqueduct, and insulation material characteristics. The proposed model systematically incorporates key environmental factors, including solar radiation, evaporative cooling, convective heat transfer, and wind speed effects, while establishing a coupled heat exchange framework that quantifies the thermal interactions among flowing water, aqueduct structures, and insulation materials. With regard to the characteristics of heat dissipation in the water of the overhead aqueducts, this study focuses on the effect of wind speed on the convective heat transfer process of the concrete primary liner and insulation materials. Meanwhile, the relationship between convective heat transfer coefficients of three materials, namely, rubber-plastic foam, fiberglass, and polyurethane, and wind speed was obtained through indoor experimental measurements. The actual observation data from Caohe aqueduct are used to verify the proposed water temperature model without covering insulation materials. Based on the historical meteorological data of Caohe aqueduct, the change of water temperature along the Caohe aqueduct of the South-to-North Water Diversion Central Route is predicted with different thicknesses of insulation materials. The results show that the water temperature at the exit section of the aqueduct is expected to be higher than zero degrees without ice conditions if the aqueduct is covered with a 5 cm thick polyurethane or 7 cm thick rubber-plastic layer.

Key words: *aqueduct, water temperature, wind speed, thermal insulation, convective heat transfer*

1. Introduction

The construction of water diversion projects can effectively mitigate the supply-demand imbalance of water for industrial, agricultural, and domestic use caused by continuous population growth [1]. As

important water conveyance structures, aqueducts in cold regions often face many complex and changing working conditions during winter [2]. The aqueducts in cold regions often experience problems with ice flow and ice-covered water transfers during the winter. The evolution of ice jams on the aqueduct in winter greatly affects water conveyance aqueducts. Unlike a river channel, the external surface of an aqueduct is directly exposed to the external atmosphere. Therefore, in addition to the heat exchange between the water surface and the atmosphere, the heat exchange between the water and the inner wall of the aqueduct can be significantly affected by the heat exchange between the outer wall and the atmosphere [3]. The large headroom underneath the aqueduct and the high wind speeds result in rapid temperature loss. Under persistent winter cold wave conditions, the aqueduct is highly susceptible to ice frazil and ice crystals during water conveyance in the absence of any insulation facilities. These ice frazil and ice crystals affect the water conveyance capacity of the aqueducts and may even clog barriers or critical channel sections, resulting in reduced water flow through the aqueducts.

Some theoretical models [4-6] and numerical simulations [7-9] have revealed the development of ice jams in cold regions. Many scholars [10, 11] have applied artificial neural networks and robot programming[12] to predict ice conditions and the safety of water diversion projects. In recent years, with the development of unmanned aerial vehicles (UAVs), Chen *et al*. [13] and Liu *et al*. [14] have integrated computer-based image processing with UAV-captured images to predict ice conditions and the safety of water diversion projects. Leng *et al*. [15] and Zakharova *et al*. [16] adopted satellite remote sensing to monitor ice jam conditions and verify existing ice jam models. The development of ice jams in aqueducts and natural rivers is influenced by heat exchange between the water body and the atmosphere, as well as solar radiation. Zhao *et al*. [17] proposed the components of surface heat flux, namely longwave radiation, latent heat flux, and conductive heat flux. Huokuna *et al*. [18] have proposed an equation to estimate the temperature response of rivers. Jing and Li [19] utilized simulation data for water temperature in the diversion open channel, identified air temperature, wind speed, and flow velocity as the three pivotal factors influencing the distribution of water temperature and the location of icing. Multimodal analysis of the Songhua River system, Harbin, utilizing multi-annual observational datasets, deciphered thermal synchrony between atmospheric and fluvial temperatures while quantifying the heat fluxes [20]. A process-based quantitative river temperature model (RAFT), combined with sensitivity analyses, identified the primary physical drivers of Sacramento River temperature as dam discharge temperature, air temperature, and solar radiation [21]. Recently, a heat transfer model between land, surface air, and surface water was developed with the aim of quantifying the effect of surface heat load on the runoff heating process, and the results show that the initial surface temperature is the most critical factor in the heat exchange process [22]. The melting of thick ice sheets starts mainly at the ice-water interface and is dominated by the heating of the ice sheet by solar radiation rather than by the heat flux from the underlying water column [23]. Based on flume data, Li *et al*. [24] calculated the dimensionless ice-water heat transfer coefficient to be 1.1×10^{-3}.

Thermal regime analysis of the aqueduct structure–water system often overlooks critical interdependencies between solar loading and material insulation dynamics. The water temperature model of the aqueduct differs significantly from the general channel water temperature model. In the general channel water temperature model, the water temperature is mainly affected by the ground temperature, while the temperature of the water in the overhead aqueduct is more susceptible to wind speed. Considering the unique characteristics of the diversion aqueduct, the integrated effects of complex environmental factors, including wind speed and sunshine, on the water temperature within the

aqueduct should be taken into account. This research thoroughly explores the heat dissipation law in the system consisting of water, aqueduct, and thermal insulation materials. The study results reveal the change rule of the temperature field of the aqueduct and the water in the process of winter water conveyance, providing a scientific basis for the improvement of the winter water conveyance capacity of the aqueduct in cold regions. The study findings elucidate the temperature field dynamics of both the aqueduct and its water during winter conveyance, offering a scientific foundation for enhancing the winter water conveyance capacity of aqueducts in cold regions.

2. Model Framework

There are some differences in water temperature modeling for aqueducts and channels. Typically, overhead aqueduct systems are directly exposed to the air with large headroom and high wind speeds. Therefore, the variation in wind speed, which is a key factor, has a significant effect on the heat dissipation of the aqueduct. Fig. 1 illustrates the differences between Yang's open channel model and the overhead aqueduct model [25]. In this investigation, the influences of wind speed and air temperature on the heat dissipation within the aqueduct's water will be examined, drawing upon Yang's open-channel model to understand the characteristics of temperature variations in the overhead aqueduct.

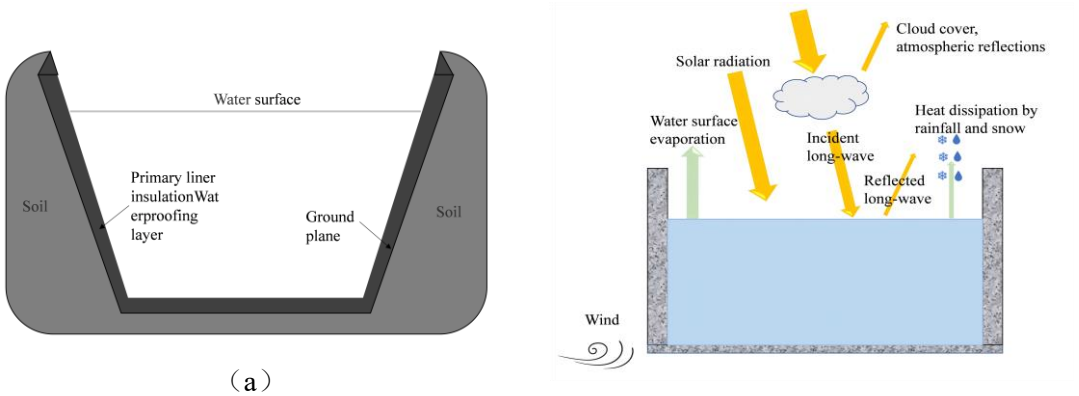

（a） （b）

Fig. 1. Comparison of open channel and aqueduct models
（a）Yang's open-channel model [25]（b）Model of an overhead aqueduct

2.1. Heat Exchange Between the Water Surface and Atmosphere

Heat exchange between the water surface and the atmosphere includes solar radiation, longwave radiation, and evaporative-convective heat exchange. Heat exchange between the water surface and the atmosphere includes solar radiation, longwave radiation, and evaporative-convective heat exchange. According to Yang's model of heat exchange between the water surface and the atmosphere [25], when the water surface temperature is equal to the atmospheric temperature, the net heat flux at the water surface can be described as:

$$\phi_{sa} = \phi_{sn} + \phi_a - \phi_b - \phi_c - h_{sa}\left(T_w - T_a\right) \quad (1)$$

where ϕ_{sa} is the net heat flux at the water surface, W·m^{-2}, ϕ_{sn} is the net heat flux from solar radiation at the water surface (no solar radiation at night, $\phi_{sn} = 0$), W·m^{-2}, ϕ_a is the net heat flux of long-wave radiation at the water surface, W·m^{-2}, ϕ_b is the net heat flux of atmospheric inverse radiation at the water surface, W·m^{-2}, ϕ_c is the evaporative heat flux at the water surface, W·m^{-2}, h_{sa} is the heat exchange

coefficient between the water surface and the atmosphere (for Beijing, Baoding, Shenyang, Baotou areas: $h_{sa}=10(1+V_z)$, V_z is the wind speed), T_w is water temperature, °C, and T_a is the atmospheric temperature, °C.

Through thermodynamic synthesis integrating three foundational models: the solar radiation model [26], the parameterized general model of water ice and snow [27], and the Angström insolation percentage model [28], the net heat flux of solar radiation at the surface is expressed as:

$$\varphi_{sn}=I_0E_0\sin\alpha\left(0.126+0.648\left(1-C^2\right)\right)(1-\alpha_s) \quad (2)$$

$$\alpha_s=\begin{cases}0.0564/\alpha & \alpha\geq 0.105rad\\ 0.537-4.408(\alpha-0.105) & \alpha<0.105rad\end{cases} \quad (3)$$

where I_0 is a solar constant, taken as 1367 W·m^{-2}, E_0 is the correction coefficient for the sun-earth distance, which can be calculated according to the Technical Specification for Observation and Assessment of Solar Energy Resources (DB52T 1396-2018), a is the solar altitude angle, which is the angle between the direction of incidence of sunlight and the earth's plane, rad, C is the cloudiness, for which a value of 0.21 is adopted specifically for the Baoding region in Hebei, and a_s is the albedo of solar radiation at the water surface.

Technical Specification for Observation and Assessment of Solar Energy Resources (DB52T 1396-2018) [26] is calculated as:

$$\begin{cases}E_0=1/\begin{pmatrix}1/1.000011+0.034221\cos\theta+0.00128\sin\theta\\ +0.000719\cos(2\theta)+0.000077\sin(2\theta)\end{pmatrix}\\ \theta=2\pi(n-1)/365\end{cases} \quad (4)$$

Using 2015-2016 winter meteorological data from Baoding, Hebei Province, China, Yang [27] derived a linearized equation representing the difference between water surface net longwave radiation flux and atmospheric counter-radiation flux.

$$\phi_a-\phi_b=-94.6-0.6T_a \quad (5)$$

When the water surface temperature equals the atmospheric temperature, based on the Russian winter evaporation formula [25] and the linear relationship between the water surface evaporation heat flux φ_c and atmospheric temperature T_a proposed by Yang [27] in China, the following equation can be obtained:

$$\phi_c=(6.04+2.9V_z)(1-R_h)\times\begin{cases}3.35+0.80T_a & -40\leq T_a\leq -10\\ 6.11+0.36T_a & -10<T_a\leq 0\\ 6.11+0.62T_a & 0<T_a\leq 10\end{cases} \quad (6)$$

where V_z is the wind speed, m·s^{-1}, and R_h is the relative humidity, which is taken as 0.4 in the Baoding area of Hebei, China.

2.2. Heat Exchange Between Aqueduct and Water

Aqueducts are typically constructed using concrete as the primary building material. Based on the basic law of heat conduction in Fourier's Law, the heat exchange between water and the external atmosphere through the aqueduct is calculated by applying the steady-state heat transfer theory of multi-layer flat walls.

$$\phi_{wb}=\sum_{j=1}^{k}k_j/h_j\left(T_c-T_a\right) \quad (7)$$

where ϕ_{wb} is the net heat flux of the channel surface, W m^{-2}, h_j is the thickness of the j layer of the aqueduct, k_j is the thermal conductivity of the layer of the aqueduct, W·m^{-2}·°C^{-1}, and T_c is the surface temperature of the aqueduct, °C.

$$\phi_{wbe} = \frac{1}{\chi}\int_0^{\chi} \phi_{wb} ds = \frac{\chi_a}{\chi} h_{wba}\left(T_w - T_c\right) + \frac{\chi_b}{\chi} h_{wbb}\left(T_w - T_c\right) = h_{wbe}\left(T_w - T_c\right) \quad (8)$$

where ϕ_{wbe} is the equivalent heat flux of heat exchange between the water and the aqueduct, W m^{-2}, χ is the wetted perimeter, m, a is the side, b is the bottom, and h_{wbe} is the equivalent heat exchange coefficient of heat exchange between the water and the aqueduct.

The heat exchange coefficient of the outer wall of the aqueduct can be calculated by

$$h_{wbj} = 1/\left(\sum_{j=1}^{k} h_j / k_j + 1/h_{wj}\right) \quad (9)$$

where h_{wj} is the convective heat exchange coefficient on the surface of the aqueduct, W·m^{-2}·°C^{-1}, and h_{wbj} the heat exchange coefficient of the outer wall of the aqueduct, W·m^{-2}·°C^{-1}.

The convective heat transfer coefficients for each wall of the aqueduct, when the aqueduct is not covered with insulation materials, can be calculated according to the Kelbeck formula [3]:

$$\begin{cases} \text{roof plate：} h_w = 3.83V_z + 4.67 \\ \text{ventral plate：} h_w = 3.83V_z + 3.67 \\ \text{base plate：} h_w = 3.83V_z + 2.1 \\ \text{inner plate：} h_w = 3.6 \end{cases} \quad (10)$$

where h_w is the convective heat transfer coefficient, W·°C^{-1}.

The convective exchange between the water and the externally applied thermal insulation materials for aqueducts can be described as:

$$h_{wbi} = 1/\left(\sum_{j=1}^{k+1} h_j / k_j + 1/h_{wi}\right) \quad (11)$$

where 1 in k+1 represents the thermal insulation material, h_{wbi} is the heat exchange coefficient of the outer surface of the thermal insulation material, W·m^{-2}·°C^{-1}, and h_{wi} is the convective heat exchange coefficient of the surface of the thermal insulation material, W·m^{-2}·°C^{-1}.

2.3. Prediction of Water Temperature along the Aqueduct

Under the assumption of thermal equilibrium between surface and bulk water temperatures, and applying Yang's [25] one-dimensional open-channel thermal model while neglecting in-water thermal diffusion terms, we derive:

$$\frac{dT_w}{dt} = \frac{B\phi_{sa} - \chi\phi_{wbe}}{\rho C_p A} \quad (12)$$

Substituting $\frac{dx}{dt} = V$ into Eq. (13), we obtain:

$$\frac{dT_w}{dx} = \frac{B\phi_{sa} - \chi\phi_{wbe}}{\rho C_p A V} \quad (13)$$

From Eqs. (1) and (10), the heat exchange between the water and atmosphere is given as:

$$B\phi_{sa} - \chi\phi_{wbe} = B\phi_{sa\,0} - \left(Bh_{sa} + \chi h_{wbe}\right)\left(T_w - T_a\right) \quad (14)$$

According to the integral variation of Eqs. (19) and (20), the longitudinal variation of the temperature of the aqueduct is given by:

$$\begin{cases} when: B\phi_{sa0}-(T_w-T_a)(Bh_{sa}+\chi h_{wbe})>0: \quad T_w=T_a+\dfrac{B\phi_{sa0}-\exp\dfrac{-(Bh_{sa}+\chi h_{wbe})x+y_1}{\rho C_p AV_w}}{Bh_{sa}+\chi h_{wbe}} \\ when: B\phi_{sa0}-(T_w-T_a)(Bh_{sa}+\chi h_{wbe})<0: \quad T_w=T_a+\dfrac{B\phi_{sa0}+\exp\dfrac{-(Bh_{sa}+\chi h_{wbe})x+y_2}{\rho C_p AV_w}}{Bh_{sa}+\chi h_{wbe}} \end{cases} \tag{15}$$

where y_1 is a constant: $y_1=\rho C_p AV\ln\left(B\phi_{sao}-(T_{w0}-T_a)(Bh_{sa}+\chi h_{wbe})\right)$, y_2 is a constant: $y_2=\rho C_p AV\ln\left(-B\phi_{sao}+(T_{w0}-T_a)(Bh_{sa}+\chi h_{wbe})\right)$. ρ is the density of water, kg/m^3, C_p is the specific heat capacity of water, J·kg^{-1}·°C^{-1}, B is the width of the water surface, m, X is the length from the inlet of the aqueduct, m, A is the cross-sectional area of the aqueduct, m^2, and V_w is the flow velocity of the water, m · s^{-1}. The net heat flux at the surface of the water can be expressed by $\phi_{sa0}=\phi_{sn}+\phi_a-\phi_b-\phi_e$ [27].

2.4. Measurement of Convective Heat Transfer Coefficient for Thermal Insulation Material

When insulation materials are externally applied to aqueduct surfaces, they establish direct thermal contact with the ambient atmosphere, creating a convective boundary condition. As aqueducts are typically elevated structures, the convective heat transfer between their exterior insulation and ambient air is particularly susceptible to wind velocity variations beneath the span. Hu *et al*. [29] proposed that the convective heat transfer coefficient is linearly related to the wind speed:

$$h_w=c+dV_z \tag{16}$$

where c and d are two constants.

In order to obtain the relationship between the heat dissipation coefficient of the insulation material and the wind speed, this study experimentally measured the temperature at different insulation materials and wind speeds.

2.4.1 Experimental Setup

The experimental setup in this study is shown in Fig. 2. The axial fan SF-4-2R was used to provide a controllable wind source, and a heavy-duty inverter EV8100-2.2G was used to adjust the fan speed to obtain different wind speeds for the experiment. Wind speed and air temperature were measured using an HT-9829 thermal anemometer, with temperature and wind speed measurement accuracies of ±1 °C and ±0.02 m/s, respectively. To establish the required thermal conditions for experimental validation, two 40 × 20 cm electric heating foils were mounted on the rear side of the insulation material. These heating elements were connected to a regulated power supply SPS-E305 DC (0-30 V, 0-5 A) to enable controlled surface heating and facilitate adiabatic treatment implementation. The mean value acquired from two measurement points was adopted as the representative surface temperature. An HT-9815 thermocouple thermometer was employed to measure the surface temperature of the insulation material, featuring a measurement accuracy of ±(0.15% of the measured reading +1 °C). This device can be used not only to measure the surface convective heat transfer coefficient of thermal insulation materials, but also to determine that of solar panels. The solar panel is fixed by a support bracket, and the influence of wind speed at different installation angles on its surface convective heat transfer coefficient is tested. Based on the measured results, the optimal installation angle of solar panels can be determined.

For this experiment, three commonly used engineering insulation materials were selected: rubber-

plastic plates, fiberglass, and polyurethane, all of which are widely applied in modern applications. These insulation materials were cut into samples of 40 × 40 cm with a thickness of 2 cm. Two vacuum insulation panels measuring 50 × 50 cm with a thickness of 2 cm were selected as the insulation material. These panels were then wrapped with insulating black thermal PVC tape, forming the insulation material test device as illustrated in Fig. 2.

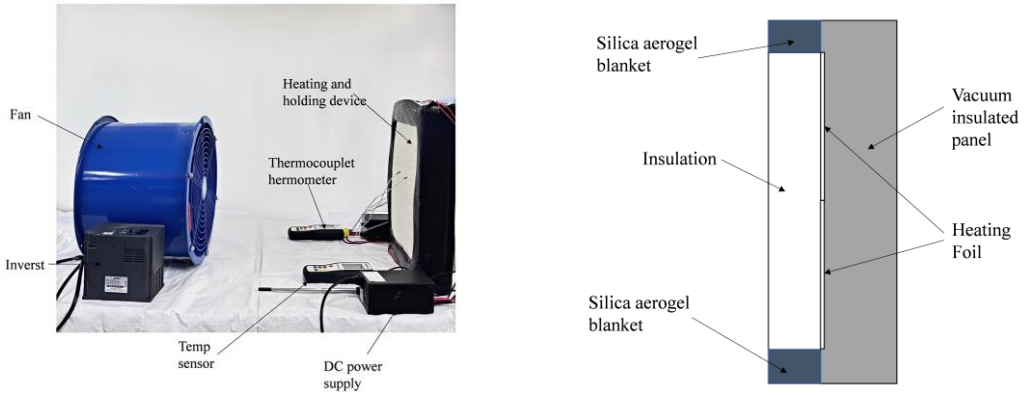

（a） （b）

Fig. 2. Test equipment and schematic diagram
(a) Test equipment (b) Schematic diagram of the heating and holding device

2.4.2 Experimental Methods

According to Newton's Law of Cooling, the total transferred heat power is calculated as follows [29]:

$$Q = h_w A_m \left(T - T_a\right) = UI \tag{17}$$

where Q is the power of the heating wire, W, h_w is the convective heat transfer coefficient, $W \cdot m^{-2} \cdot °C^{-1}$, A_m is the upper surface area of the insulation material, m^2, T is the temperature of the insulation material, °C, and T_a is the ambient temperature at the time of the experiment, °C, U *and* I are the voltage and current used to heat the thermocouple, respectively.

The average heat flux q_{mw}, local heat conduction flux q_{condx}, and local convective heat flux q_{convx} of the insulation are calculated as follows [30]:

$$q_{mw} = \frac{Q_{mw}}{A_m};\ q_{condx} = \frac{\lambda}{\delta}\left(T - T_s\right) \tag{18}$$

$$q_{convx} = q_{mw} - q_{condx} \tag{19}$$

where A_m is the surface area of the insulation material, m^2, λ is the thermal conductivity of the insulation material, $W \cdot m^{-2} \cdot °C^{-1}$, δ is the thickness of the insulation material, m, and T_s is the outer surface temperature of the insulation material, °C.

The local convection heat transfer coefficient h_w can be expressed as:

$$h_w = \frac{q_{convx}}{T_s - T_a} \tag{20}$$

where T_a is the ambient temperature, °C, at the time of the experiment.

2.4.3 Experimental Results

In practical engineering, thermal insulation materials are laid on the lower surface of the aqueduct.

Since the relative orientation between the wind direction and the thermal insulation material is not fixed, two representative working conditions are selected for this study, namely the scenario where the wind direction is parallel to the plane of the thermal insulation material, and the scenario where the wind direction is perpendicular to the plane of the thermal insulation material. The convective heat transfer coefficients of the insulation surfaces were calculated for different wind speeds. Finally, the relationship between wind speed and the convective heat transfer coefficient of the insulation material was derived by linear fitting, and the experimental and linear fitting results are shown in Fig. 3. The data presented in Figure 3 were derived from experimental measurements, including the inner and outer surface temperatures of the thermal insulation material, wind speed, electric current, and voltage. The raw data were first recorded and computed in Excel, then imported into Origin software for plotting and linear fitting.

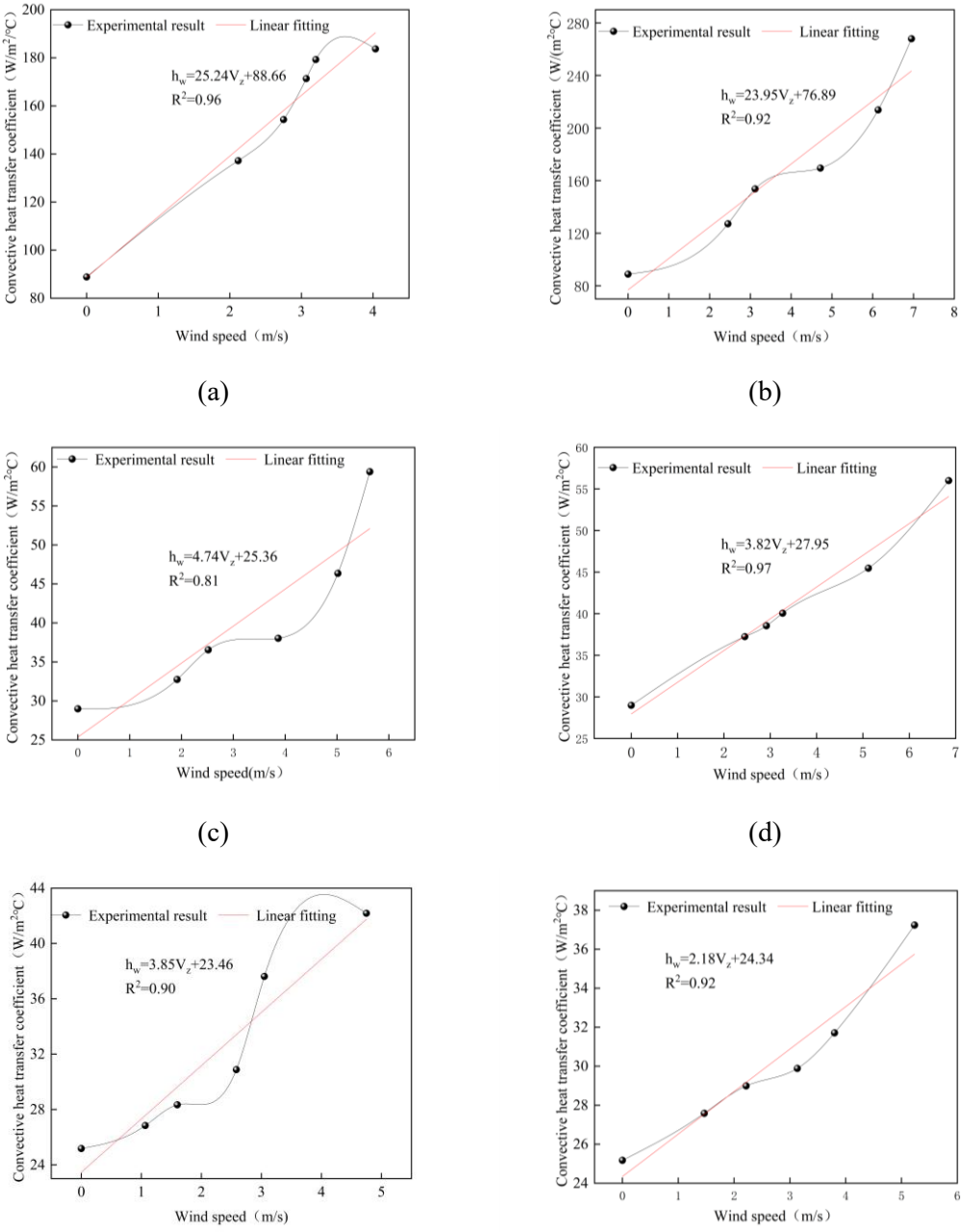

Fig. 3. The relationship between the convective heat transfer coefficient and wind speed under different conditions. (a) Polyurethane plane perpendicular to wind direction; (b) Polyurethane plane parallel to wind direction; (c) Rubber-plastic plate plane perpendicular to the wind direction; (d)Rubber-plastic plate plane parallel to the wind direction; (e) Fiberglass plane perpendicular to wind direction; (f) Fiberglass plane parallel to wind direction

From the analysis of the data in Fig. 3, it can be concluded that as the wind speed increases, the convective heat transfer coefficient of the three kinds of thermal insulation materials increases, with the polyurethane plane perpendicular to the wind direction having the greatest influence. Comparative analysis under controlled wind conditions reveals the polyurethane surface's convective heat transfer coefficient to be markedly greater than that of rubber-plastic and fiberglass materials. Polyurethane exhibits lower local heat conduction flux at comparable thicknesses due to its markedly inferior thermal

conductivity relative to rubber-plastic and fiberglass materials. In addition, the experimentally measured outer surface temperature of polyurethane is lower than that of the rubber-plastic plate and fiberglass when the inner surface temperature of the insulation material is the same. According to Eq. (20), the surface convective heat transfer coefficient of polyurethane is higher than that of the other two groups of materials.

Thermal deformation at 100 °C (manifesting as central bulging) is the principal cause of the compromised linear fitting when the rubber-plastic plate is oriented perpendicular to wind flow. This bulge may lead to errors in the surface temperature measurement and thus affect the linear fitting effect. Linear regression analysis yields superior fitting results for polyurethane and fiberglass, as neither material exhibits observable thermal deformation (i.e., mid-section bulging) during the heating process. In this experiment, thermocouple probes from the HT-9815 thermocouple thermometer were adhesively bonded to both the inner and outer surfaces of the thermal insulation specimens, enabling real-time monitoring of the temperature difference and temperature variation patterns across the two surfaces.

During the experiment, heating of the rubber-plastic board induced internal heat transfer and accumulation, which in turn caused bulging deformation in the central region of the insulation material. This deformation resulted in localized detachment of the insulation from the heating foil, disrupting their intimate thermal contact. The resulting obstruction of heat transfer and delayed temperature conduction meant that the temperature data captured by the thermocouple probes failed to accurately represent the true temperatures of the insulation material and the heating foil, ultimately causing a marked degradation in temperature measurement accuracy and adversely affecting the reliability of subsequent analytical results. The thermal conductivity of the fiberglass is slightly higher than that of the rubber-plastic plate, while the experimentally measured convective heat transfer coefficient is lower than that of the rubber-plastic plate. The positional relationship between the wind direction and the plane of the insulation material affects the convective heat transfer coefficient between the insulation material and the air. When the wind direction is perpendicular to the plane of the insulation material, the effect of the wind speed on the convective heat transfer coefficient of the surface of the insulation material is greater than when the two are parallel.

3. Model Validation and Application

3.1. Project Profile

This study validates the proposed model by examining the Caohe aqueduct along the Central Route of the South-to-North Water Diversion Project as a case study to investigate the water temperature variations. The dimensions of the single-span aqueduct are 6.0 × 5.4 m, and it has a maximum width of 30 m. The maximum height of the ground level of the aqueduct is 15 m, and the design flow rate is 125 $m^3 \cdot s^{-1}$. The flow rate can be increased to 150 $m^3 \cdot s^{-1}$ in case of need. The aqueduct maintains a typical cross-sectional span of approximately 22 m, with a designed water depth of 4.15 m. The thickness of the side wall of the aqueduct is 0.6 m, and the thickness of the bottom plate is 0.5 m. In order to enhance the structural stability of the aqueduct, the side wall of the aqueduct is equipped with side beams, and a transverse beam is added at the top, both of which are 0.5 m wide.

3.2. Model Validation

The water temperature model is validated by using the field measurement data of the Caohe River aqueduct in the South-to-North Water Diversion Central Route Project. According to the data on January

16, 2024, the water depth of Caohe aqueduct was 3.45 m, and the water flow velocity was 0.86 $m \cdot s^{-1}$. Wind speed and ambient air temperature at the Caohe aqueduct site were continuously monitored using a Testo 405i instrument, with specified accuracies of ±0.5 ℃ for temperature and ±0.03 m/s for wind speed, between 15:00 and 16:00. The monitoring frequency was 1 s. The data of air temperature and wind speed are shown in Fig. 4. Fig. 4 demonstrates that the ambient air temperature oscillates within a range of 2–7 °C while exhibiting a gradual decreasing trend. Meanwhile, the wind speed fluctuates between 0.2 and 1.2 $m \cdot s^{-1}$.

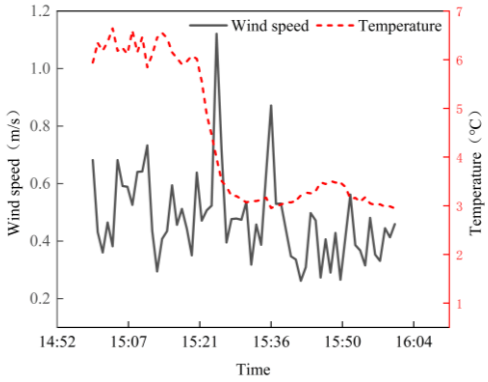

Fig. 4. Plot of temperature and wind speed monitoring data

In Fig. 5 in the manuscript, the inlet water temperature adopts measured data from 15:00 to 15:22. According to the measured flow velocity, the total travel time of water from the aqueduct inlet to the outlet is calculated to be 44 minutes and 34 seconds. Therefore, the outlet water temperature in Fig. 5 is the measured data collected from 15:44 to 16:02. The water temperature varies slightly as water flows from the inlet section to the outlet section. This is mainly attributed to the small temperature difference between air and water, which results in low heat loss during water flow. Fig. 5 illustrates significant temperature variations occurring between 15:00 and 15:22, accompanied by continuous wind speed fluctuations. Subsequently, the numerically computed water temperatures were compared against in-situ measurements collected by an RBR solo³ compact temperature logger (accuracy: ±0.002 ° C) over the corresponding monitoring period. The comparison results are presented in Fig. 5.

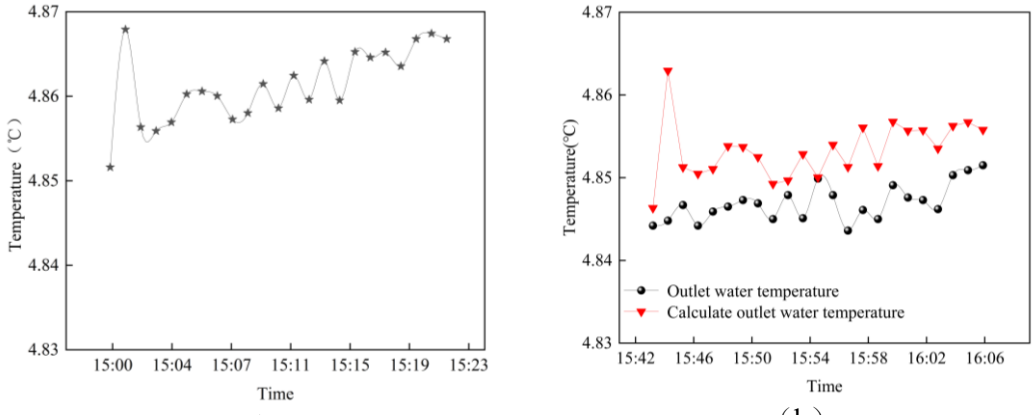

（a） （b）

Fig. 5. Comparison of measured water temperature at the inlet and outlet sections with calculated water temperature at the outlet section. (a) Measured water temperature at the inlet section; (b) Comparison between the calculated and measured water temperatures at the outlet section

As shown in Fig. 5, the calculated and actual measured outlet section water temperatures are generally lower than the actual measured inlet section temperatures and vary with the inlet section water

temperatures. This can be attributed to the absorption of heat from solar radiation in the atmosphere by the water as it flows from the inlet section of the aqueduct to the outlet section. In addition, when the atmospheric temperature is higher than the water temperature, the total amount of solar radiation heat absorbed by the water is less than the total amount of heat emitted through various mechanisms. These heat dissipation mechanisms include evaporation, convective heat dissipation, inverse radiation heat dissipation between the surface of the water and the atmosphere, and heat dissipation between the water and the aqueduct. The calculated outlet section water temperatures are generally higher than the actual measured outlet section water temperatures. This phenomenon is due to the model assumption that the solar radiation covers the entire water surface uniformly. Field observations indicate the aqueduct tank's elevation exceeds the water surface level, creating potential shadow effects due to solar incidence angles and inter-aqueduct angular relationships. The measured outlet section water temperatures are compared and analyzed with the calculated outlet section water temperatures. The measured and calculated water temperatures at the outlet section exhibited consistent trends during the observation period, demonstrating good agreement between experimental data and model predictions. As solar altitude decreases in the afternoon, the temperature differential between measured inlet and calculated outlet sections exhibits a progressive increase, correlating with declining ambient temperatures. This observed trend aligns with fundamental thermodynamic principles.

3.3. Analysis of the Effect of External Thermal Insulation Materials

Based on the environmental conditions during a cold snap in January 2016, the ambient temperature reached a minimum of -18.6 °C, and the inlet water temperature of the aqueduct was 0.1 °C. At that time, the current speed was 0.86 m s^{-1}, and the wind speed at the Caohe aqueduct was 2.4 m·s^{-1}. During normal operation, the water level in the aqueduct was maintained at 4.15 m. The aqueduct is made of concrete material, which has a density of 2515 kg·m^{-3}, a thermal conductivity of 2.98 W·m^{-1}·°C^{-1}, and a specific heat capacity of 967.2 J·kg^{-1}·°C^{-1}. Based on the ambient temperature during the nighttime cold wave in January 2016, the proposed water temperature model is used to calculate the change in water temperature in the aqueduct under the coverage of different insulation materials. These calculations provide a theoretical basis for the development of the winter insulation scheme for this project. This study examines four thermal insulation scenarios for the Caohe Aqueduct's exterior surface during winter conditions: (1) no thermal insulation, and insulation layers of (2) 3 cm, (3) 5 cm, and (4) 7 cm thickness. When the computed water temperature falls below 0 °C, the system determines ice conditions.

Based on the calculation results, it can be concluded that under cold weather conditions, the temperature of the water in the aqueduct may be reduced to 0°C during its flow from the inlet section to the outlet section. The lowered temperature significantly elevates the freezing potential, resulting in ice formation that could obstruct the aqueduct and impair its hydraulic conveyance capacity. The model predictions indicate that despite applying 3 cm thick insulation layers (fiberglass, rubber-plastic composite, or polyurethane) to the aqueduct's exterior surface, the outlet section exhibits persistent ice formation and inadequate thermal insulation performance. The highest water temperature in the outlet section appears when the aqueduct is covered with polyurethane. On this basis, the calculation results take into account the case of 5 cm of insulation layers outside the aqueduct. The model predictions indicate that 5 cm insulation layers (rubber-plastic plate or fiberglass) fail to prevent ice formation at the exit section. However, the water temperature at the outlet section is higher than 0 °C in the case of the polyurethane insulation layer, which indicates that its thermal insulation effect is better. Calculated data indicate that the 7 cm fiberglass insulation applied to the aqueduct's outer surface fails to prevent ice

formation at the exit section, demonstrating inadequate thermal performance. Covering the aqueduct with a 7 cm polyurethane and rubber molding board can achieve a good insulation effect. The polyurethane insulation effect is better than that of the rubber-plastic plate. Based on the calculated results, the 5 cm-thick polyurethane insulation outperforms the 7 cm rubber-plastic sheet in thermal insulation performance. Taking both the thermal protection effect on water inside the aqueduct and economic benefits into consideration, it is recommended to apply a 5 cm polyurethane insulation layer to the outer surface of the aqueduct.

4. Conclusions

This study focuses on the water temperature evolution and freeze protection of overhead aqueducts. Its core contribution is the development of a water temperature prediction model embedded with a coupled heat exchange framework covering the water body, aqueduct structure, and thermal insulation material. The model comprehensively accounts for the structural features of overhead aqueducts as well as the impacts of key environmental factors, including wind speed and solar radiation.

The proposed model is validated using field measurement data from the Caohe Aqueduct on the Middle Route of the South-to-North Water Diversion Project. Verification results show that the water temperature calculated by the model is in good agreement with field measurements, confirming the model's accuracy and practical applicability.

Based on the validated model, this study reveals that the water in the Caohe Aqueduct faces ice formation risk under cold weather conditions. To address winter icing hazards, thermal insulation coverage on the aqueduct's outer surface is proposed as a mitigation measure, and the thermal performance of different insulation schemes is quantitatively evaluated. Model calculations indicate that neither 30 mm nor 50 mm thick insulation layers (glass fiber or rubber-plastic cladding) can provide sufficient thermal resistance to prevent ice accretion at critical sections. By contrast, both 5 cm thick polyurethane insulation and 7 cm thick rubber-plastic plates can maintain the aqueduct’s outlet water temperature above 0 °C, and 5 cm polyurethane achieves better thermal insulation performance than 7 cm rubber-plastic plates.

Furthermore, experimental research on thermal insulation materials supplements the mechanism-level findings of this work. It is found that polyurethane has the largest surface convective heat transfer coefficient, followed by rubber-plastic plates, while glass fiber has the smallest. In addition, the relative orientation between wind direction and the insulation material plane exerts a notable influence on the convective heat transfer coefficient between the insulation surface and ambient air. Specifically, when the wind direction is perpendicular to the insulation plane, wind speed imposes a more pronounced effect on the surface convective heat transfer coefficient of the insulation material.

Overall, the modeling method and quantitative conclusions presented in this study can provide a theoretical basis and engineering reference for the thermal design and anti-freezing renovation of overhead water conveyance aqueducts.

Acknowledgements

This research is supported by the National Key Research and Development Program (No. 2022YFC3202500), the National Natural Science Foundation of China (Nos. 52479096, U2443221), the Key Laboratory of Rock Mechanics and Geohazards of Zhejiang Province (No.ZJRMG-2023-03), the State Key Laboratory of Safety and Health for Metal Mines (2023-JSKSSYS-01), the Fundamental

Research Funds for the Central Universities (No. JZ2022HGTB0273), and Innovation and entrepreneurship funds for returnees of Hefei. These supports are gratefully acknowledged.

References

[1] Long, D., *et al*., South-to-North Water Diversion stabilizing Beijing's groundwater levels, *Nature Communications*, 11 (2020), 1, p.3665.

[2] Xu, Z., et al., Application of real-time water temperature prediction system in winter for long-distance water diversion projects, *Journal of Hydroinformatics*, 26 (2024), 4, pp.915-933.

[3] Yang, K., Heat exchange of water and spatial-temporal variation of water temperature and ice content in aqueduct, *Journal of Hydraulic Engineering*, 53 (2022),11, pp.1317-1327. (in Chinese)

[4] Wazney, L., *et al*., Numerical simulation of river ice cover formation and consolidation at freeze-up, *Cold Regions Science Technology*, 168 (2019), p.102884.

[5] Liu, M., *et al*., Regulating a Long-Distance Canal System with Floating Ice Cover in the Winter, *Journal of Cold Regions Engineering*, 29 (2015), 1, p.04014009.

[6] Sohrabi, M. M., *et al*., Estimation of daily stream water temperatures with a Bayesian regression approach, *Hydrological Processes*, 31 (2017), 9, pp.1719-1733.

[7] Xu, Z., *et al*., Emergency intervention modes for ice jam events in large-scale water diversion projects, *Hydrology Research*, 54 (2023), 10, pp.1134-1151.

[8] Zhai B., *et al*., A numerical model for river ice dynamics based on discrete element method, *Journal of Hydraulic Research*, 61 (2023), 3, pp.369-381.

[9] Batina, J., Peyrous, R., Study on the possibility of maintaining ice in an ice hole using numerical modeling of phase change and meteorological digitized data, *Heat Mass Transfer*, 61 (2025), 3, pp.1-30.

[10] Guo, X., *et al.*, Ice-Jam Forecasting during River Breakup Based on Neural Network Theory, *Journal of Cold Regions Engineering*, 32 (2018), 3, p.04018010.

[11] Zhang, S., *et al*., Multi-source data fusion method for structural safety assessment of water diversion structures, *Journal of Hydroinformatics*, 23 (2021), 5, pp. 249–266.

[12] Kowshal, A., *et al*., Ice-jam flood predictions using an interpretable machine learning approach, *Environmental Modelling & Software*, 192 (2025), p.106534.

[13] Chen, J., Liu, D., Using computer vision to monitor ice conditions in water supply infrastructure: a study of salient image features, *Journal of hydroinformatics*, 25 (2023), 4, pp.1139-1152.

[14] Liu, D., *et al*., Dynamic BIM-augmented UAV safety inspection for water diversion project, Computers in Industry, 108 (2019), pp.163-177.

[15] Leng, Y., *et al*., Detailed Classification of River Ice Types Using Sentinel-2 Imagery: A Case Study of the Inner Mongolia Reach of Yellow River, *Remote Sensing*, 18 (2026), 5, p.672.

[16] Zakharova, E., *et al*., Satellite Altimetry Over Frozen Rivers. Satellite Altimetry and Hydrodynamic Model Reproduce the Ice Jam Conditions, *Advances in Space Research*, 77 (2025),4, pp.4352-4363.

[17] Zhao, S., *et al*., Wintertime Surface Heat Exchange for the Inner Mongolia Reach of the Yellow River, *Journal of the American Water Resources Association*, 56 (2020), pp.348 - 356.

[18] Huokuna, M., *et al*., Ice in reservoirs and regulated rivers, *International Journal of River Basin Management*, 20 (2022),1, pp.1-16.

[19] Jing, H.F., Li, C. G., Applications of Water Temperature Models to Water Diversion Open Channels, *Advanced Materials Research*, 550 (2012), pp. 2595-2599.

[20] Song, X.C., Jing, L., Annual Observations of Climatic Impacts in the Songhua River Basin, China, *Advances in Meteorology*, 2015 (2015), 1, p.138436.
[21] Daniels, M.E., Danner, E.M., The Drivers of River Temperatures Below a Large Dam, *Water Resources Research*, 56 (2020), 5, p.026751.
[22] Luo, Y., *et al*., Urban Surface Thermal Runoff Generation Mechanism and Scenario Simulation, *Water Resources Research*, 59 (2023), 4, p.033881.
[23] Dombrovsky, L.A., Kokhanovsky, A.A., Solar heating of ice-covered lake and ice melting, *Journal of Quantitative Spectroscopy & Radiative Transfer*, 294 (2023), p. 108391.
[24] Li, N., *et al*., Heat transfer at ice-water interface under conditions of low flow velocities, *Journal of Hydrodynamics, Ser. B.*, 28 (2016), 4, pp.603-609.
[25] Yang, K., Water temperature models of open channels in glacial period, *Journal of Hydraulic Engineering*, 53 (2022), 01, pp.20-30. (in Chinese)
[26] He, Q., Xie, Y., Research on the climatological calculation method of total solar radiation in China, *Journal of Natural Resources*, 25 (2010), 02, pp.308-319. (in Chinese)
[27] Yang, K., Heat exchange model between river-lake and atmosphere during ice age, *Journal of Hydraulic Engineering*, 52 (2021),05, pp.556-564. (in Chinese)
[28] Ashton G. D., *River and Lake Ice Engineering*, Water Resources Publications, Littleton, Colorado, USA, 1986.
[29] Hu, W.W., *et al*., Experimental research on the convective heat transfer coefficient of photovoltaic panel, *Renewable Energy*, 185 (2022), pp. 820-826.
[30] Wu, S.Y., *et al*., Experimental investigation on convection heat transfer characteristics of flat plate under environmental wind condition, *International Journal of Green Energy*, 14 (2017), 3, pp.317-329.

Submitted: 6.03.2026.
Revised: 5.08.2026.
Accepted: 12.08.2026.